On Fault-Ride-Through Performance in MMC-HVDC Applications Controlled as a Virtual Synchronous Machine

Carolin Hirsching, Max Goertz, Simon Wenig, *Member, IEEE*, Alexander Bisseling, Michael Suriyah, *Member, IEEE*, and Thomas Leibfried, *Senior Member, IEEE*

***Abstract*—Due to decreasing inertia within the German transmission grid, HVdc transmission links are recently planned as a grid-forming asset in order to contribute to the overall system stability. Here, virtual synchronous machine implementations may be favoured as they enable inertia supply and operation at different grid strengths. However, their fault-ride-through capability is linked to several challenges such as current limitation, the preservation of transient stability and dynamic reactive current injection, especially, while providing high inertia. Moreover, diverse effects occur at the point of connection, such as voltage drop and phase jump effects, which can be traced back to the fault impedance characteristic during a symmetrical fault event and affect the transient stability. Therefore, this article investigates these occurring effects in detail. Based on this analysis, the performance of the virtual synchronous machine is evaluated with respect to different design aspects - namely the reactive power control, the inertia model and design of the phase locked loop - resulting in a recommendation for a design compromise. Finally, observed relations are classified according to their applicability within a typical design of an HVdc converter equipped with half-bridge submodules. Derived design recommendations are validated by simulations in electromagnetic transients software.**

***Index Terms*—Control design, grid-forming control, fault-ride-through, MMC-HVdc, virtual synchronous machine.**

I. Introduction

With the ongoing energy transition and an increasing share of power electronic assets, the system inertia within numerous transmission grids decreases continuously [1]. Consequently, grid-forming control concepts for different assets (e.g. HVdc converters) are required to ensure grid stability, see [1], [2].

Manuscript received 1 December 2021; revised 1 July 2022; accepted 11 August 2022. Date of publication 8 September 2022; date of current version 30 November 2022. This work was done when Max Goertz and Simon Wenig at TransnetBW, 70173 Stuttgart, Germany. Paper no. TEC-01319-2021. *(Corresponding author: Carolin Hirsching.)*

Carolin Hirsching, Alexander Bisseling, Michael Suriyah, and Thomas Leibfried are with the Institute of Electric Energy Systems and High-Voltage Technology, Karlsruhe Institute of Technology (KIT), 76131 Karlsruhe, Germany (e-mail: carolin.hirsching@kit.edu; alexander.bisseling@kit.edu; michael.suriyah@kit.edu; thomas.leibfried@kit.edu).

Max Goertz and Simon Wenig are with the Mosaic Grid Solutions, 76131 Karlsruhe, Germany (e-mail: m.goertz@mosaic-gridsolutions.com; s.wenig@mosaic-gridsolutions.com).

Color versions of one or more figures in this article are available at https://doi.org/10.1109/TEC.2022.3205055.

Digital Object Identifier 10.1109/TEC.2022.3205055

In light of these developments, several grid-forming control methods were presented in literature, for instance, a frequency-power-droop control, matching control, direct voltage control as well as virtual synchronous machine (VSM) implementations [3]. According to the classification in [4], some of the grid-forming control implementations in literature aim to form an islanded ac grid, whereas other implementations enable smooth operation even if other synchronous units (e.g. generators or additional grid-forming units) are present.

Focusing on the applicability for a grid-forming asset connected to a widespread ac grid, the latter type of controls appears more suitable. Here, VSM implementations may be advantageous in terms of inertia supply and the ability to operate in densely meshed ac grids as well as in islanding mode [5], [6], [7], [8], [9], [10]. For instance, the implementation introduced in [5] for modular multilevel converter (MMC) applications makes use of an inertia model related to the swing equation of a synchronous generator, whereas a phase locked loop (PLL) is applied to emulate the mechanical damping properties of a synchronous generator within the inertia model.

A key issue for the control design represents the fault-ride-through capability during ac contingencies (ac-frt) such as three-phase (3 ph) faults [2]. The requirements and challenges regarding grid-forming applications are summarized by the following four points: i) instantaneous dynamic reactive current injection in positive sequence according to related standards [11], ii) adherence to given technical constraints of installed power electronics. Therefore, total current injection is limited and prioritization of the reactive current component might be required resulting in a sudden operation point adaption of active power quantities, iii) a dynamic response of active power, however, stands in contrast to high inertia supply as high inertia is linked to reduced power synchronization dynamics and finally, iv) high inertia supply as well as current limitations result in a conflict with the VSM's transient stability [12], [13], [14], [15].

Besides the mentioned challenges, an adequate evaluation of active and reactive power quantities is required in order to determine meaningful statements regarding further control design requirements. Therefore, [16] specifies the evaluation of active and reactive power or current quantities extracted from the fundamental phasor components in positive sequence as introduced in [17].

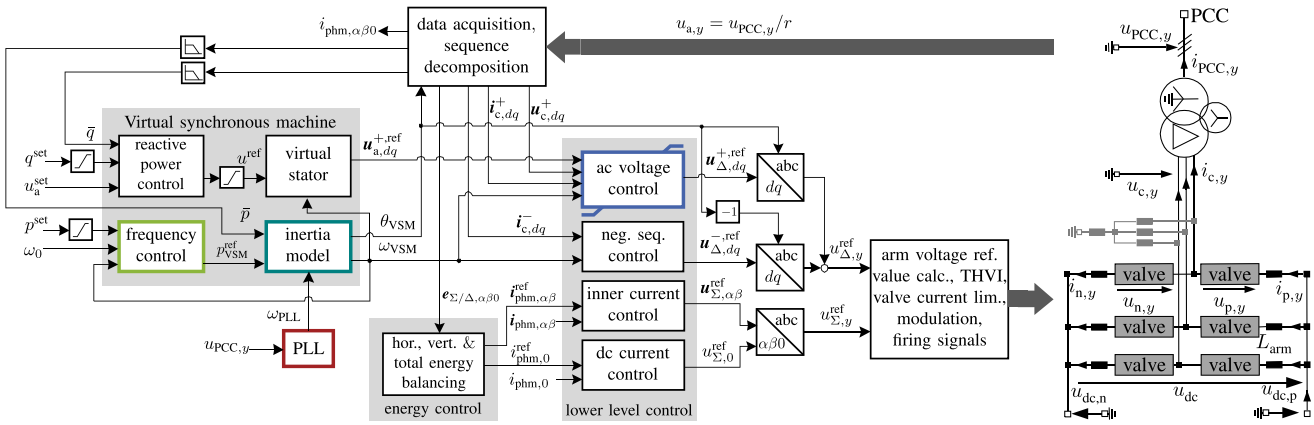

Fig. 1. Overview of control scheme for an MMC controlled as a VSM.

Now, regarding the first mentioned challenge, the required response of reactive current is the straight-forward consequence of a grid-forming asset to a drop in system voltage. However, when evaluating fundamental components, additional effects are revealed that may lead to an undesired initial behaviour after fault occurrence, for instance, a decrease of reactive current injection that is traced back to the fault impedance characteristic. Therefore, this paper contributes to understand occurring effects during 3ph-faults in a first stage revealing additional requirements in control design regarding the dynamics of reactive power control, active power reference tracking as well as the PLL.

It is important to highlight that the PLL is only considered to emulate the angular speed of the VSM stator i.e. the MMC does not change into grid-following mode during fault events. However, [18] has recently proven that utilization of a PLL for additional damping of the angular speed deviation improves the transient stability of a VSM during large disturbances. In addition to this finding, the authors observed that the inertia model and the PLL design influence each other in a sensitive manner, whereas both degrees of freedom may contribute to overcome issues regarding an undesired instantaneous reactive power response after fault occurrence. To the author's best knowledge, there is a lack of required design recommendations in literature, as the effect might remain undetected when utilizing common measurement techniques for active and reactive power or current quantities.

In light of the described observations, this contribution focuses on the fault-ride-through (frt) performance of VSM implementations and is structured as follows: Section II describes the considered VSM control concept for MMC-HVdc applications equipped with half-bridge submodules. This includes implemented measures to avoid loss of synchronization when the converter operates in current limiting mode. Section III gives a profound overview on occurring effects during 3ph-faults, whereas Section IV provides control adaptions for improvement of the ac-frt performance including a dynamic reactive power controller as well as an analysis of the impact of PLL design and the inertia model. Moreover, the control design problem of the VSM is evaluated in Section V providing a PLL design recommendation, whereas introduced measures are validated by a case study fulfilling the above mentioned challenges. Section VI concludes the paper.

II. MMC Controlled as a VSM

An overview of the considered electrical and control model is depicted in Fig. 1. Each valve consists of 224 half-bridge submodules with an average submodule voltage of 2.5 kV and is considered as a *Type-4* detailed equivalent circuit model according to [19]. With the aim to conduct adequate ac fault studies in EMT software, special attention has to be paid on the required depth of modelling. According to [20], the phenomena investigated within this paper are classified within the range of temporary and slow-front overvoltages. Here, a compromise between modeling depth and computation efficiency is made and the reader is referred to [21] for more details regarding the utilized electrical model.

A. Control Overview

The control scheme in Fig. 1 reveals a quasi-decoupled control approach of ac, dc as well as converter internal dynamics. Here, difference and sum quantities are introduced for each phase $y \in \{1, 2, 3\}$ according to (1) and (2), as carried out extensively in [19], [22] and [23].

$$i_{\mathrm{phm},y} = \frac{i_{\mathrm{p},y} + i_{\mathrm{n},y}}{2}, \qquad i_{\mathrm{c},y} = i_{\mathrm{n},y} - i_{\mathrm{p},y}. \tag{1}$$

$$u_{\Delta,y} = \frac{u_{\mathrm{n},y} - u_{\mathrm{p},y}}{2}, \qquad u_{\Sigma,y} = \frac{u_{\mathrm{p},y} + u_{\mathrm{n},y}}{2}. \tag{2}$$

The considered VSM concept consists of an inertia model, a frequency control, reactive power control and a virtual stator impedance, similar to [5] and [7]. The ac side controls are realized in a synchronous reference frame (SRF) rotating at virtual angular speed ω_{VSM}. The transformation angle θ_{VSM} for dq-quantities is provided by the inertia model depicted in Fig. 2. In this contribution, the ac side control concept refrains from traditional current controllers. Instead, an ac voltage control similar to [24] with current limiting capability is taken into account for the positive sequence as explained in Section II-C. The controlled voltage is defined as $u_{\mathrm{a}} = u_{\mathrm{PCC}}/r$ considering

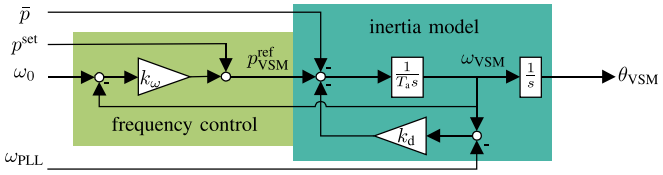

Fig. 2. VSM implementation with primary droop control and inertia model related to the swing equation of a synchronous generator.

TABLE I
PARAMETER SET FOR CONSIDERED ± 262.5 kV MMC-HVDC LINK

Parameter	Value
rated power of link P_r	1.05 GW
rated reactive power Q_r	440 Mvar
rated dc voltage (pole-to-pole) U_{dc}	525 kV
rated ac voltage (valve / grid side)	280 kV / 400 kV
nominal grid frequency f_0	50 Hz
short circuit level / X/R ratio ac grid	45 GVA / 10
transformer leakage reactance	20 %
number of submodules per valve arm	224
submodule capacitor	8.5 mF
arm inductance L_{arm}	50 mH

the transformer ratio r derivable from Table I. For sake of completeness, a negative sequence control is implemented to provide grid services according to [11] and may be utilized to avoid dc oscillations during unbalanced grid conditions as suggested in [8]. As indicated in Fig. 1, the control approach comprises an energy-based control methodology for circulating and dc current quantities considering horizontal, vertical as well as total energy balancing controls similar to [23].

Arm reference voltages are calculated from $u^{\text{ref}}_{\Sigma,y}$ and $u^{\text{ref}}_{\Delta,y}$ utilizing (2). Moreover, third harmonic voltage injection (THVI) as well as a valve current limitation algorithm is applied before reference signals are transferred towards the modulation layer.

B. VSM Model

For the following explanations, we define the complex space-vectors $\boldsymbol{x}_{dq} := x_d + jx_q$ and $\boldsymbol{x}_{\alpha\beta} := x_\alpha + jx_\beta$ for any quantity x. Derivable from Fig. 2, the considered inertia model emulates the swing equation of a synchronous generator according to (3). For realization of the inertial damping by k_d, the VSM concept makes use of a PLL determining the angular speed of the grid ω_{PLL}. The idea of ω_{PLL} is to model the angular speed of the virtual stator apart from its nominal angular speed $\omega_0 = 2\pi f_0$. Hence, the feedback path with k_d damps differences between the virtual rotor and estimated grid frequency, and not differences between virtual rotor and nominal grid frequency. This approach allows for a more realistic modeling of a virtual synchronous machine during transient events. Moreover, steady-state frequency deviations in the overlaid transmission grid are considered in a simple manner within the inertia model. Angle synchronization to the grid is realized by the power imbalance between power reference $p^{\text{ref}}_{\text{VSM}}$ and the low-pass filtered active power quantity $\bar{p}$. In addition, a frequency droop control is realized by means of

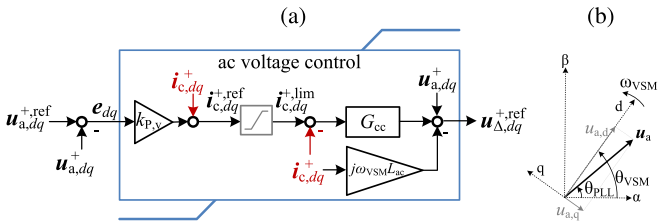

Fig. 3. (a) ac voltage control with current limitation scheme, (b) vector diagram defining VSM-SRF.

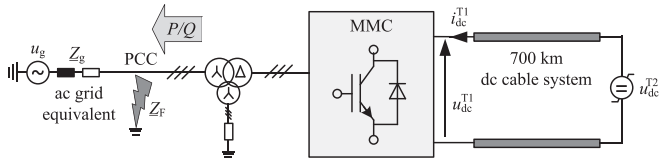

Fig. 4. ±262.5 kV HVdc transmission scheme in symmetric monopolar configuration, fault location f-3 ph in the vicinity of the VSM-controlled station T1.

k_ω. The inertial time constant corresponds to $T_a = 2HS_r/\omega_0$.

$$\frac{d\omega_{\text{VSM}}}{dt} = \frac{1}{T_a}\Big(\underbrace{p^{\text{set}} + k_\omega(\omega_0 - \omega_{\text{VSM}})}_{:=p^{\text{ref}}_{\text{VSM}}} - \bar{p} - k_d(\omega_{\text{VSM}} - \omega_{\text{PLL}})\Big) \tag{3}$$

The amplitude of the internal VSM voltage u^{ref} is determined by a reactive power controller G_Q according to (4) combined with a set point feed-forward of the nominal grid voltage amplitude u^{set}_a. Here, $\bar{q}$ represents the low-pass filtered reactive power quantity.

$$u^{\text{ref}} = u^{\text{set}}_a + G_Q(q^{\text{set}} - \bar{q}) \tag{4}$$

A virtual stator impedance is considered in order to determine current dependent voltage references $\boldsymbol{u}^{+,\text{ref}}_{a,dq}$ for ac voltage control. This is important to enable the VSM to operate at strong grid conditions [25] and is realized by a quasi-stationary (QS) implementation according to (5).

$$\boldsymbol{u}^{+,\text{ref}}_{a,dq} = u^{\text{ref}} - (R_v + j\omega_{\text{VSM}}L_v)\boldsymbol{i}^{+,\text{ref}}_{c,dq} \tag{5}$$

The choice of the QS implementation instead of a dynamic one is motivated by investigations provided in [10]. A dynamic stator implementation may lead to an oscillatory behaviour of currents at marginal grid voltage deviations if small values are chosen for the virtual stator resistance. On the other hand, increasing the virtual resistor leads to an undesired coupling between active and reactive power quantities.

C. Ac Voltage Controller Considering Current Limitation

Fig. 3 shows the block diagram of the considered ac voltage controller with an inner current limiting capability. In the first section, a proportional gain $k_{P,v}$ is applied to regulate the voltage error $\boldsymbol{e}_{dq}$ combining a feed-forward of measured current quantities $\boldsymbol{i}^{+}_{c,dq}$. The output of this part determines current references $\boldsymbol{i}^{+,\text{ref}}_{c,dq}$ which are passed through a current limitation scheme resulting in $\boldsymbol{i}^{+,\text{lim}}_{c,dq}$. The second part represents a conventional current controller $G_{cc} = k_{P,cc} + k_{i,cc}/s$.

If the current limitation block is inactive, measured current quantities are removed from the overall transfer behaviour of the controller (highlighted red in Fig. 3(a)) and the ac voltage controller can be summarized to $k_{\mathrm{P,v}} G_{\mathrm{cc}} \boldsymbol{e}_{dq} + ff$. Here, ff combines the feed-forward terms at the output of G_{cc}. If the limitation block is active, the condition $\boldsymbol{i}_{\mathrm{c},dq}^{+,\mathrm{lim}} < \boldsymbol{i}_{\mathrm{c},dq}^{+,\mathrm{ref}}$ becomes valid. I.e. $\Delta \boldsymbol{i}_{\mathrm{c},dq}^{+,\mathrm{ref}} = \boldsymbol{i}_{\mathrm{c},dq}^{+,\mathrm{ref}} - \boldsymbol{i}_{\mathrm{c},dq}^{+,\mathrm{lim}}$ resulting in an overall behaviour of the ac voltage controller described by $k_{\mathrm{P,v}} G_{\mathrm{cc}} \boldsymbol{e}_{dq} - G_{\mathrm{cc}} \Delta \boldsymbol{i}_{\mathrm{c},dq}^{+,\mathrm{ref}} + ff$. In other words, as soon as the current limitation block is activated, the considered ac voltage control structure inherently subtracts an additional current control path that regulates $\Delta \boldsymbol{i}_{\mathrm{c},dq}^{+,\mathrm{ref}}$ to zero, whereas the MMC remains in grid-forming control mode.

D. Overall Current Limitation Scheme

Limitation of the MMC valve currents are realized by a coordinated current limitation scheme for decoupled current quantities in positive and negative sequence considering a worst case superposition, see [23].

The parallelism to synchronous generators involves that severe faults may lead to the loss of synchronous stability within grid-forming applications [13], whereby current limitation algorithms may even contribute to this tendency as shown e.g. in [12], [14]. Therefore, currents are mainly limited within the outer control loops by limitation of voltage as well as power set points. Consequently, this measure avoids potential wind-up effects evoked by the instantaneous current limitation within the ac voltage controller.

Inspired by [12], the voltage setpoint is limited by $\hat{u}_{\mathrm{a}} + X_{\mathrm{ac}} \hat{i}_c^{\max}$ according to the maximum permissible amplitude of the converters ac current $\hat{i}_c^{\max}$, whereas X_{ac} corresponds to the filter inductance of the transformer and half of arm inductance. Moreover, power references are limited by $\hat{s}^{\max} = \frac{3}{2} \hat{u}_{\mathrm{a}} \hat{i}_{\mathrm{c}}^{\max} \geq \sqrt{(q^{\mathrm{lim}})^2 + (p^{\mathrm{lim}})^2}$ with q^{lim} and p^{lim} representing the limited set points of q^{set} and p^{set}, respectively.

Derivable from Fig. 3(b), the d-axis of the VSM is not aligned to the grid voltage. Therefore, active and reactive current quantities cannot be approximated by the dq-current components within the VSM reference frame. Instead, limits are calculated utilizing measured grid voltage dq-quantities. Here, a power factor based instantaneous current limitation is chosen to maintain grid-forming functionalities according to [16] without prioritization of active or reactive current parts. However, if an ac fault occurs, a transition to reactive current prioritization might be required.

III. Challenges During 3ph-Faults

For the following investigations, a ± 262.5 kV HVdc link in symmetric monopolar configuration is taken into account as depicted in Fig. 4. The design parameters of the underlying transmission scheme are listed in Table I emphasizing the investigations at strong grid conditions. A detailed MMC and VSM control model is implemented for station T1 as introduced in the previous section. If not stated differently, related control parameters are summarized in Table II. As ac-frt events are of main interest within this contribution, the cable terminal is connected to a controlled voltage source u_{dc}^{T2} with respect to dc side controls and dc current limits at station T2. All evaluated curves are measured at station T1.

TABLE II
Control Design Parameters

G_{Q}	0.08 + 0.5/s	k_{d}	1150 p.u.
T_{a}	2· 0.1 s	k_{ω}	9 p.u.
$k_{\mathrm{P,v}}$	0.02	G_{cc}	80 + 200/s
X_{v}	$(2 \cdot 10^{-6} + j0.22)$ p.u.	k_Q^{dyn}	1 p.u.

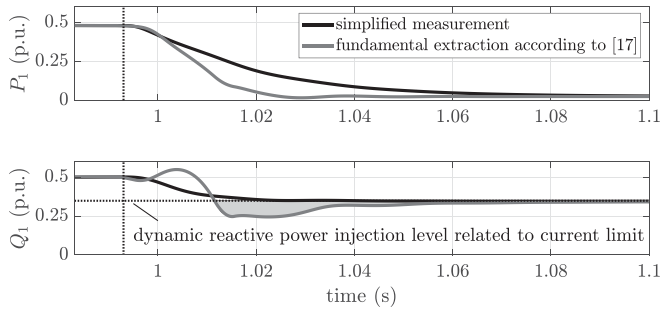

Fig. 5. Response of power quantities to a 3ph-fault with 0.15 p.u. residual grid voltage comparing different measurement methodologies.

A. Evaluation of Power Quantities

In order to harmonize the evaluation of the frt performance, special attention is paid to the determination of power quantities at evaluation node PCC in a first step. Fig. 5 shows the response of the VSM controlled MMC to a symmetric fault with 0.15 p.u. residual voltage. The fault onset is marked as a vertical line, as for all transient responses shown within this contribution. The curves designated with *simplified measurement* reflect the determination of power quantities considering all spectral components of instantaneous PCC currents and voltages with respect to a smoothing transducer delay (20 ms). The other curves show power quantities extracted from the fundamental components (currents$_{(1)}$ and voltages$_{(1)}$) by means of Fourier series similar to (6) and subsequent transformation into positive sequence as specified in [16] and introduced in [17]. Here, window T correlates to $1/f_{(1)}$, whereas $f_{(1)}$ is determined by a PLL with a time constant of 200 ms according to [16].

$$\Re\left\{U_{y,(1)}\right\} = +\frac{\sqrt{2}}{T} \int_{t-T}^{t} u_y(t) \cos\left(2\pi f_{(1)} t\right) \mathrm{d}t \tag{6a}$$

$$\Im\left\{U_{y,(1)}\right\} = -\frac{\sqrt{2}}{T} \int_{t-T}^{t} u_y(t) \sin\left(2\pi f_{(1)} t\right) \mathrm{d}t \tag{6b}$$

When evaluating the fundamental components, it is observed that the VSM response shows an undesired behaviour after fault occurrence, for instance, an adverse reactive power injection as visualized by a grey shaded area in Fig. 5. Certainly, this effect remains undetected if considering simplified power measurement techniques. However, active and reactive power quantities are only transferred at fundamental frequency and, hence, solely these spectral components contribute to stabilizing (or destabilizing) the grid during the fault. This underlines the

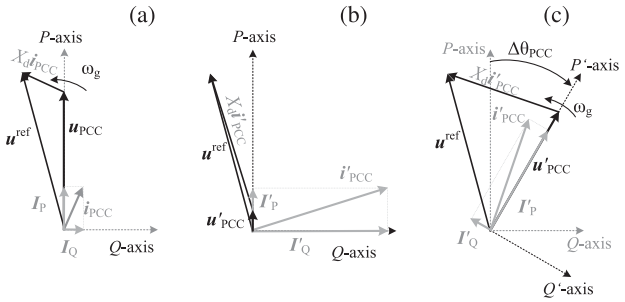

Fig. 6. Simplified vector diagrams (a) at steady-state operation, (b) after a voltage drop in u_{PCC}, (c) after a negative phase jump in u_{PCC}.

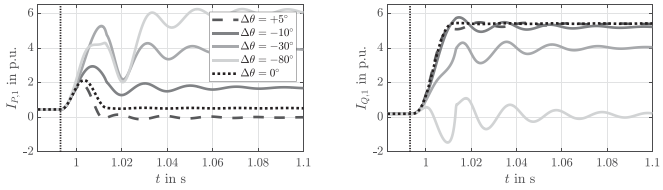

Fig. 7. Transient response of an ideal voltage source with fixed amplitude and angle to a 3-ph-fault with 0.15 p.u. residual grid voltage and different *phase jump effects*.

importance of evaluating fundamental components and requires further analysis regarding the VSM's response.

B. Fault Characteristic Analysis

At fault instant diverse effects arise within the considered system that explain the observed response behaviour and require further discussion. In simple terms, the resulting voltage during a 3ph-fault is estimated by $u'_{\mathrm{PCC}} = \underline{Z}_{\mathrm{F}}/(\underline{Z}_{\mathrm{F}} + \underline{Z}_{\mathrm{g}})u_{\mathrm{g}}$, see Fig. 4. Now, assuming the VSM acts as an ideal voltage source, the voltage at the PCC changes to u'_{PCC} immediately after fault instant. The resulting voltage u'_{PCC} depends on $|\underline{Z}_{\mathrm{g}}|$ and $|\underline{Z}_{\mathrm{F}}|$, whereas a phase jump may occur depending on the relation of real and imaginary parts between the two impedances. The VSM's transient behaviour is derivable by means of the differential equation given by (7). Here, R_{d} and L_{d} combine ohmic and inductive parts of the VSM's ac and virtual impedances, respectively.

$$R_{\mathrm{d}} i_{\mathrm{PCC}} + L_{\mathrm{d}} \frac{\mathrm{d}i_{\mathrm{PCC}}}{\mathrm{d}t} = u^{\mathrm{ref}} - u'_{\mathrm{PCC}} \tag{7}$$

For clarification of the triggered transition behaviour from steady-state to quasi-stationary inter-fault operation point, the occurring effects are now simplified in separate vector diagrams as shown in Fig. 6. Here, it is assumed that $i)$ the internal VSM voltage u^{ref} remains in its steady-state (see Fig. 6(a)) i.e. the VSM acts as an ideal voltage source, $ii)$ quasi-stationary inter-fault operation point is already achieved and $iii)$ current limits are neglected. Impedance X_{d} combines X_{ac} and the virtual impedance X_{v}.

As a consequence of a voltage drop (see Fig. 6(b)), mainly the reactive current part I'_Q is increasing which obviously explains the request for dynamic current injection according to related standards [11].

If $\Im\{\underline{Z}_{\mathrm{F}}\}/\Re\{\underline{Z}_{\mathrm{F}}\} < \Im\{\underline{Z}_{\mathrm{g}}\}/\Re\{\underline{Z}_{\mathrm{g}}\}$, a negative phase jump arises in u_{PCC} with a corresponding vector diagram in Fig. 6(c). The reaction to such kind of event is an increase of the active current component I'_P and a decrease in reactive current I'_Q that may even lead to a change in direction of flow. For $\Im\{\underline{Z}_{\mathrm{F}}\}/\Re\{\underline{Z}_{\mathrm{F}}\} > \Im\{\underline{Z}_{\mathrm{g}}\}/\Re\{\underline{Z}_{\mathrm{g}}\}$ a positive phase jump arises resulting in an opposite behaviour i.e. an increase of reactive current and decrease in active current. All described effects hold true irrespective of the pre-fault operation point.

Comparing occurring effects, a positive phase jump theoretically contributes to the desired frt behaviour. However, it is assessed rather negligible in grids with high X/R ratios, as occurring phase jumps are within a single-digit degree range.

In order to understand the system's transition behaviour caused by the aforementioned effects, the transient response of an ideal voltage source to a fault with a residual voltage of 0.15 p.u. is shown in Fig. 7. Here, different $\Im\{\underline{Z}_{\mathrm{F}}\}/\Re\{\underline{Z}_{\mathrm{F}}\}$ are taken into account resulting in different phase jumps at the PCC. Hence, for the shown faults, both – the voltage drop as well as a phase jump effect – affect the transition behaviour to the inter-fault operation point. Faults with resulting phase jumps are compared with a fault solely causing a voltage drop (see dotted graph), i.e. $\Im\{\underline{Z}_{\mathrm{F}}\}/\Re\{\underline{Z}_{\mathrm{F}}\} = \Im\{\underline{Z}_{\mathrm{g}}\}/\Re\{\underline{Z}_{\mathrm{g}}\}$ and $\Delta\theta = 0°$.

Classifying a fault with $\Im\{\underline{Z}_{\mathrm{F}}\}/\Re\{\underline{Z}_{\mathrm{F}}\} \ll \Im\{\underline{Z}_{\mathrm{g}}\}/\Re\{\underline{Z}_{\mathrm{g}}\}$, e.g. $\Delta\theta = -80°$, the dilemma of counteracting reactions in the reactive power component is emphasized resulting in the divergent instantaneous behaviour shown in Fig. 5 and Fig. 7. This effect is mainly traced back to the *negative phase jump effect*. However, with the implemented current limitation scheme (prioritization of reactive current during voltage drop contingencies) the VSM's response may segue into the desired transition behaviour as the *voltage drop effect* prevails (compare Fig. 5).

Evaluating the inequality condition $\Im\{\underline{Z}_{\mathrm{F}}\}/\Re\{\underline{Z}_{\mathrm{F}}\} < \Im\{\underline{Z}_{\mathrm{g}}\}/\Re\{\underline{Z}_{\mathrm{g}}\}$, the worst case *negative phase jump effect* arises for a purely ohmic fault impedance. However, the more significant the voltage drop at the PCC, the higher the resulting negative phase jump.

In addition to the significance of the fault, the transition behaviour strongly depends on the VSM's control dynamics. Therefore, further adaptions in control design are motivated to improve the frt performance with respect to potentially occurring effects during a 3ph-fault.

IV. Control Adaptions for Improvement of Frt Performance

Generally, the *voltage drop effect* is the main problem the converter has to cope with during ac faults, especially if the fault occurs in a greater distance of the PCC. Therefore, the dynamics of control value u_{Δ} following u^{ref} are enhanced in the first stage. Moreover, the active current component $I_{\mathrm{P,1}}$ might be reduced in consequence to stick to the dynamic current limits which represents a sudden change in setpoint. On the other hand, the initial response of active power quantities is mainly affected by the dynamics of the considered inertia model. Therefore, an option to improve active power reference tracking without

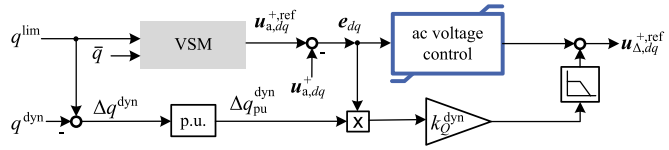

Fig. 8. Dynamic reactive power control.

changing the inertia dynamics is chosen. Moreover, special attention is paid to how the PLL design impacts the VSM's response during the fault.

A. Improvement of Reactive Power Dynamics

The response of reactive power depends on the dynamics of reactive power control, cascaded virtual stator impedance model as well as ac voltage controller. In order to improve the tracking of the reactive power at simultaneous compliance with the valve current limits, several measures are implemented.

First, q^{set} requires a temporary adaption to q^{lim} related to the desired reactive power injection level guaranteeing adequate functionality of the current limitation scheme. Moreover, an additional dynamic reactive controller (DQC) is implemented. Unlike to the stationary reactive power controller (SQC), the measured reactive power quantity is now filtered by an LPF with a bandwidth 10 times higher, hence, representing a dynamic reactive power quantity q^{dyn}. The DQC is realized as depicted in Fig. 8. Herefore, the additional control path is implemented that bypasses the virtual stator impedance achieving dynamic voltage references in dq-frame that are related to the dynamic reactive power error Δq^{dyn} and are fed-forward to the output of the normal ac voltage controller with respect to a tuning constant k_Q^{dyn}. I.e. the ac voltage control dynamics are instantaneously increased related to Δq^{dyn}.

Recalling the considered voltage controller and an event where current limitation is activated, the overall transfer behaviour of the ac voltage controller is adapted to $(k_{\text{P,v}}G_{\text{cc}}+k_Q^{\text{dyn}}F_{\text{uQ}}\Delta q_{\text{pu}}^{\text{dyn}})\boldsymbol{e}_{dq} - G_{\text{cc}}\Delta\boldsymbol{i}^{+,\text{ref}}_{\text{c},dq} + ff$ with low-pass filter F_{uQ} and $\Delta\boldsymbol{i}^{+,\text{ref}}_{\text{c},dq} = \boldsymbol{i}^{+,\text{ref}}_{\text{c},dq} - \boldsymbol{i}^{+,\text{lim}}_{\text{c},dq}$. Consequently, the current limiting capability of the overall structure remains, whereas tracking of the reactive power set point is improved at the same time. Moreover, the impact of $k_Q^{\text{dyn}}F_{\text{uQ}}\Delta q_{\text{pu}}^{\text{dyn}}$ decreases when q^{dyn} approaches q^{lim}.

The proposed idea stands in contrast to implementations shown in [14] utilizing a more dynamic control without virtual stator impedance model in steady-state and a threshold virtual impedance for current limiting purposes. Nonetheless, the proposed method may be more feasible as $i)$ the current limiting capability is given without threshold activation and $ii)$ no further knowledge about the connected grid impedance is required to guarantee effective current limitation.

B. Improvement of Active Power Dynamics

In order to support sudden changes in the power setpoint, [9] proposes a feed-forward of an estimated active power angle (PFF). This is realized by a small-signal approximation of the power transfer function resolved by angle δ_{PFF} according to (8). Here, u^{ref} represents the internal VSM voltage related to voltage set point limitations as described in Section II-D.

$$\delta_{\text{PFF}} \approx \frac{2}{3}\frac{X_{\text{d}}}{u^{\text{ref}}\hat{u}_{\text{a}}}p^{\text{ref}}_{\text{VSM}} = k_{\text{PFF}}p^{\text{ref}}_{\text{VSM}} \tag{8}$$

The advantage of this method is that the tracking of the power reference is improved without modification of inertial dynamics.

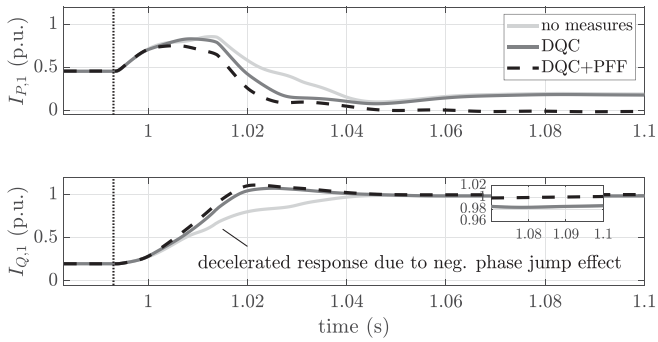

Fig. 9. Impact of active and reactive power reference tracking on the response of a VSM controlled MMC station to a 3-phase fault with 0.15 p.u. residual grid voltage and a moderate negative phase jump effect with $\Delta\theta_{\text{PCC}} = -10°$.

C. Impact of Power Reference Tracking

Fig. 9 shows the response to a symmetrical fault with 0.15 p.u. residual voltage with the aim to investigate the impact of introduced control adaptions. As faults with negative phase jumps were found to have the most critical impact on the reactive current response, a fault impedance with $3\Im\{\underline{Z}_{\text{F}}\}/\Re\{\underline{Z}_{\text{F}}\} = \Im\{\underline{Z}_{\text{g}}\}/\Re\{\underline{Z}_{\text{g}}\}$ is chosen resulting in $\Delta\theta_{\text{PCC}} = -10°$. Regarding the reactive current response, mainly the DQC measure contributes to the improvement of dynamic response, i.e. this measure enables that $I_{Q,1}$ reaches ≈ 1 p.u. within ≈ 20 ms. This represents a reduction in rise time of 46 % or rather duplicated response dynamics. The main impact of the PFF measure is described by removing the inter-fault steady-state offset of $I_{P,1}$ (as derivable from the vector diagram in Fig. 6(b)) resulting in an enhanced reactive current injection capability by additional $\approx 2\,\%$. Comparing the phase jump related responses in Fig. 7, the PFF measure gets even more important with increasing *negative phase jump effects*.

It is worth mentioning that - at the cost of less damped overshoots - the transient response of reactive current injection may be even improved by further tuning of k_Q^{dyn}. However, if the fault impedance characteristic leads to a more severe *negative phase jump effect*, i.e. the fault impedance is more ohmic, special attention has to be paid on how to resolve occurring angle stability issues. Therefore, the impact of PLL design is further analyzed within this contribution.

D. Impact of Frequency Tracking on VSM Response

The challenge to overcome an undesired behaviour related to the *negative phase jump effect* can be clarified by the reactive

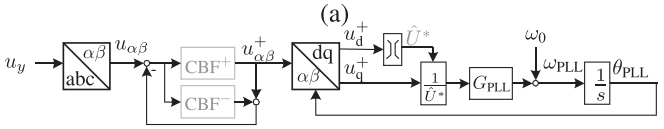

Fig. 10. Generalized CBF-PLL structure with amplitude normalization scheme.

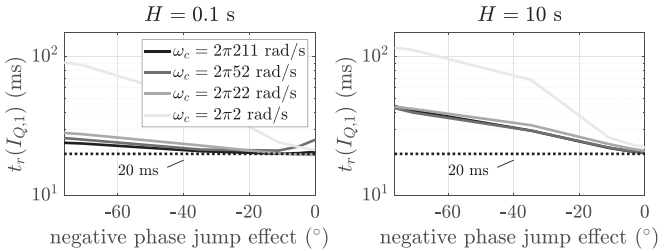

Fig. 11. Rise time t_r (90%) of reactive current response after fault occurrence comparing different PLL bandwidths and different inertia constants H.

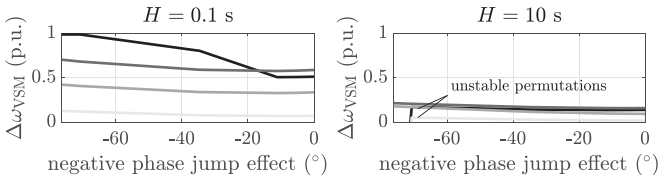

Fig. 12. Deviation of virtual angular speed after fault occurrence comparing different PLL bandwidths and different inertia constants H. Legend see Fig. 11.

power flow equation in (9).

$$q = \frac{3}{2}\frac{\hat{u}_\text{a}}{X_\text{d}}\left(u^\text{ref}\cos\left(\theta_\text{VSM} - \theta_\text{PCC}\right) - \hat{u}_\text{a}\right) \tag{9}$$

During pre-fault steady-state conditions, $|\theta_\text{VSM} - \theta_\text{PCC}|$ is rather small and the approximation for small angles holds true. Now, if θ_PCC jumps into negative direction with $|\Delta\theta_\text{PCC}| > 2|\theta_\text{VSM} - \theta_\text{PCC}|$, subsequent to a related contingency within the grid, $|\theta_\text{VSM} - \theta_\text{PCC}|$ increases resulting in a decreased impact of u^ref. Consequently, dynamics of reactive power injection will improve if θ_VSM follows $\Delta\theta_\text{PCC}$ quickly. For this purpose, the implemented inertia model is rewritten in Laplace domain in (10).

$$\omega_\text{VSM} = \frac{p^\text{set} - \bar{p} + k_\omega\omega_0}{T_\text{a}s + k_\text{d} + k_\omega} + \underbrace{\frac{k_\text{d}}{T_\text{a}s + k_\text{d} + k_\omega}}_{H_\omega}\omega_\text{PLL} \tag{10}$$

Note that $\omega_\text{VSM} = \dot{\theta}_\text{VSM}$. Hence, regarding the first term, increasing k_d or decreasing H will result in a faster compensation of the angle error via the power synchronization term $p^\text{set} - \bar{p}$. Evaluating the second term, the frequency (and phase) response is linked to the PLL dynamics. Within this contribution, a two-module complex-bandpass filter (TM-CBF) structure is considered as depicted in Fig. 10 [26] and is utilized for sequence decomposition purposes by means of CBF$^+$ and CBF$^-$ for positive and negative sequence, respectively. The PLL transfer behaviour is represented by $\omega_\text{PLL} = H_\text{PLL}\omega_\text{PCC}$ according to [27]. H_ω represents a low-pass filter linked to the inertia model. The primary frequency control parameter

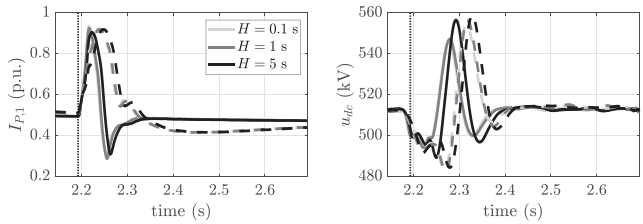

Fig. 13. Response to a phase angle step of $\Delta\vartheta = -10°$ at grid equivalent comparing different inertia dynamics for $\omega_c(H_\text{PLL}) = 2\pi 22$ rad/s (solid) and $\omega_c(H_\text{PLL}) = 2\pi 5$ rad/s (dashed).

k_ω is not regarded as a tuning parameter as power-frequency droop factors may be subject to related grid codes. Moreover, the damping coefficient k_d is chosen relatively high in order to improve transient damping [18]. Assuming $k_\omega \ll k_\text{d}$ the cutoff frequency of H_ω correlates to k_d/T_a, see Table II. At normal grid conditions $\omega_\text{PLL} = \omega_0$ including the predominant steady-state offset within the grid. Therefore, the PLL does not impact the VSM's steady-state properties [18].

For transient events, increasing the bandwidth ω_c of the PLL results in an increased contribution of PLL dynamics to the inertia model and therefore a more dynamic frequency (and phase) tracking resulting in a decreased impact of the power imbalance term in (10). Therefore, an evaluation of the resulting design problem is further motivated and discussed in the sequel.

V. Evaluation of Design Problem

Figs. 11 and 12 show the impact of the *negative phase jump effect* for different PLL designs and negligible inertia ($H = 0.1$ s) as well as high inertia ($H = 10$ s) during a 3ph-fault with 0.15 p.u. residual voltage. Here, the rise time t_r of reactive current to 90 % of the inter-fault steady-state value as well as the resulting deviation in virtual angular speed $\Delta\omega_\text{VSM}$ are evaluated. Resulting phase jumps reach from $\Im\{\underline{Z}_\text{g}\}/\Re\{\underline{Z}_\text{g}\} = \Im\{\underline{Z}_\text{F}\}/\Re\{\underline{Z}_\text{F}\}$ to a worst case of a purely ohmic fault impedance ($\approx -80°$ within the considered setting). *Positive phase jump effects* are not regarded within this evaluation as their potential extent is rather negligible within the given setting. The results are obtained by post-processing of extensive numerical simulations. All stable design permutations were validated for preservation of valve current limits during any kind of event according to guidelines for grid-forming applications [16] including operability in islanding mode.

It is shown that for very slow PLL dynamics (e.g. $\omega_c = 2\pi 2$ rad/s), there is a very high impact of the fault impedance characteristic on the VSM's response irrespective of implemented inertia H. This may even lead to a negative reactive current injection after fault instant (as derivable from Fig. 5). Therefore, it is not recommended to utilize PLL implementations with $\omega_c(H_\text{PLL}) \ll \omega_c(H_\omega)$.

Increasing the PLL bandwidth results in an improved response behaviour after fault occurrence, whereas low inertia implementations show far lower impact related to the *negative phase jump effect* with a worst case of ≈ 25 ms rise time for the considered permutations. However, the optimized response behaviour in low inertia applications is at the cost of high frequency deviations

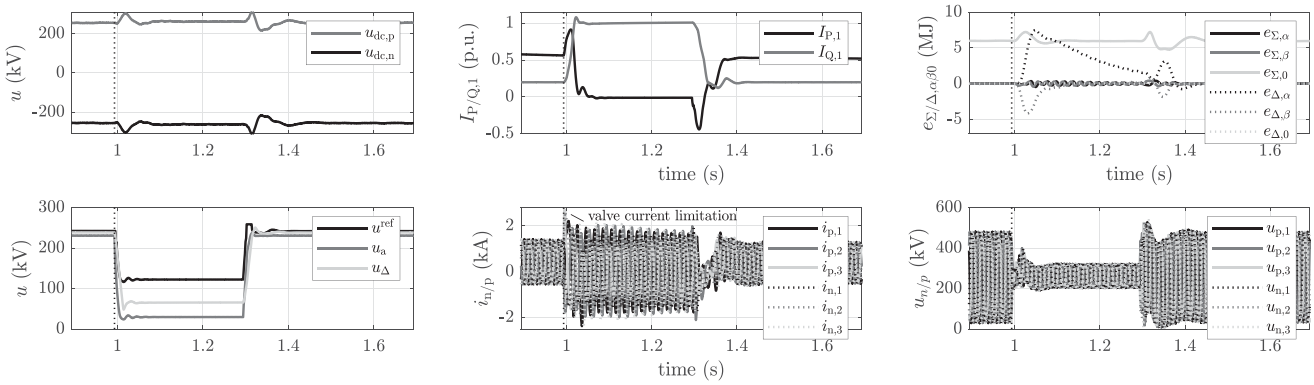

Fig. 14. Response to an ac-frt event with 0.15 p.u. residual voltage and resulting $\Delta\theta_{\text{PCC}} = -30°$ with moderate inertia ($2H = 2$ s) and a PLL design according to the introduced design recommendation.

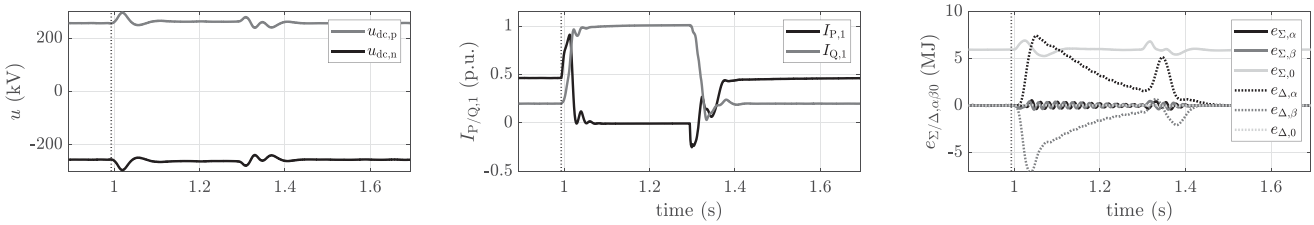

Fig. 15. Response to an ac-frt event with 0.15 p.u. residual voltage and resulting $\Delta\theta_{\text{PCC}} = -60°$ with moderate inertia ($2H = 2$ s) and a PLL design according to the introduced design recommendation.

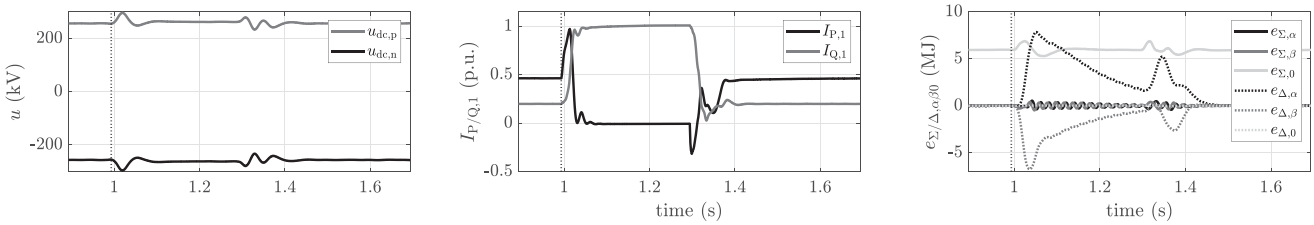

Fig. 16. Response to an ac-frt event with 0.15 p.u. residual voltage and resulting $\Delta\theta_{\text{PCC}} = -80°$ with moderate inertia ($2H = 2$ s) and a PLL design according to the introduced design recommendation.

(up to approximately 1 p.u.) which are almost independent of the occurring phase jump effect. This is traced back to the fact that increasing inertia correlates with an improved frequency stability and vice versa [15].

Consequently, increasing inertia highly reduces the resulting frequency deviations. However, there are unstable permutations for high phase jumps if $\omega_c(H_{\text{PLL}}) \ll \omega_c(H_\omega)$ or $\omega_c(H_{\text{PLL}}) \gg \omega_c(H_\omega)$. The PLL design challenge may be transferred into a second order control problem. In light with the elaborated consumptions, a PLL bandwidth of $\omega_c(H_{\text{PLL}})$ beeing approximately 1.7-3.7 times higher than $\omega_c(H_\omega)$ is found as a compromise between optimized inertia supply, damping of resulting frequency deviations, sufficient disturbance rejection capability within the PLL as well as reactive current injection dynamics.

In the next step, recommendations for PLL design are evaluated with respect to resulting acdc interactions at a $-10°$ phase jump event during steady-state. Fig. 13 shows the corresponding response to such an event comparing different inertia constants as well as PLL designs. Clearly, the area below $I_{\text{P,1}}$ correlates with the energy provided by the MMC. Hence, reduced PLL and/or inertial dynamics result in higher energy queries. Here, the energy stored within the submodule capacitors is balanced via the dc side and therefore explains the resulting impact on the dc voltage.

Regarding a HB-MMC application, PLL design as well as inertia supply has to be chosen carefully in order to guarantee safe operation during such an event i.e. $u_{\text{dc}} > 2\hat{u}_{\text{c}}$. Of course, the interaction between ac and dc side may be reduced by increasing the number of submodules i.e. the available buffering energy per arm. However, within the considered hardware design, the recommendation of $\omega_c(H_{\text{PLL}}) \approx \{1.7...3.7\}\omega_c(H_\omega)$ is verified, again building a compromise between inertia supply and feasible acdc interactions.

Based on the derived design recommendations, the overall frt performance of station T1 is now evaluated in Figs. 14–16 for a design compromise enabling inertia supply of $H = 1$ s. The fault impedance is designed to model a fault with 0.15 p.u. residual voltage. The fault occurs at $t_{\text{F}} = 0.993$ s and is cleared after

300 ms which is a relatively high fault duration for the severity of the fault aiming to show stable operation point recovery. A fault impedance characteristic is chosen that leads to severe *negative phase jump effects* of -30° in Fig. 14, -60° in Fig. 15 as well as a worst case of -80° for the given $|\underline{Z}_\mathrm{F}|$ in Fig. 16. As a consequence of the fault, active and reactive current components respond instantaneously in a desired manner. The instantaneous reaction of active power components increases with the severity of negative phase jump. However, instantaneous reactive current injection into negative direction is avoided even for a worst case of a purely ohmic fault, see Fig. 16. u^ref is reduced related to the ac current amplitude limitations, see Fig. 14. Therefore, instantaneous valve currents do not exceed their physical limitations. This findings hold true for $\Delta\theta = -60^\circ$ and $\Delta\theta = -80^\circ$, although not shown in Figs. 15 and 16 for sake of brevity. The difference between u^ref and control value u_Δ relates to the voltage drop across the virtual stator impedance. Total energy variations ($e_{\Sigma,0}$) as well as vertical energy drifts are compensated (e_Δ) and acdc interactions are kept within an acceptable range i.e. HB submodules are kept within safe operation. After fault clearing, the pre-fault operation point can be restored without loss of synchronization due to implemented set point adaption in voltage and power. The dynamics related to set point recovery are traced back to the PFF implementation.

VI. Conclusion

This paper provides a profound analysis of occurring effects during ac-3 ph events and evaluates the overall frt performance of a VSM with respect to inertia supply, PLL design aspects and desired dynamic response. Here, high inertia and small PLL bandwidths are more prone to an undesired frt behaviour that is traced back to the *negative phase jump effect*. Therefore, control design represents a compromise between contribution to voltage stability by means of reactive current injection and angle stability by means of inertia supply. To overcome analyzed challenges, a dynamic reactive power controller was proposed enabling to realize double high reactive power dynamics at moderate *negative phase jump effects*.

The investigations were conducted in a HB-MMC scheme with limited but realistic energetic content. Hence, it was additionally shown that contribution of a grid-forming HVdc scheme to a phase jump event is limited by the number of submodules while exhausting of the dc voltage band. Since higher PLL bandwidths were again found to have less impact on dc voltage deviations, an increased inertia supply can be realized. With respect to this conclusion, a PLL design recommendation was derived by means of extensive numeric simulations for enabling high inertia supply, whereas an improved contribution to voltage stability during ac-frt events could be realized. Finally, a case studies in electromagnetic transients software validated the derived design conclusions.

References

[1] 50Hertz Transmission GmbH, Amprion GmbH, TenneT TSO GmbH, and TransnetBW GmbH, "Assessment of system stability," *German Grid Development Plan 2023, Version 2021, 2nd draft*, 2021.

[2] M. Goertz and S. Wenig, "Grid-forming requirements for HVDC and FACTS – A TSO perspective," in *Proc. PES Gen. Meeting*, 2021, pp. 1–13.

[3] A. Tayyebi, F. D. Döfler, F. Kupzog, Z. Miletic, and W. Hribernik, "Grid-forming converters–inevitability, control strategies and challenges in future grid applications," in *Proc. CIRED Workshop*, Ljubljana, Slovenia, 2018, pp. 1–5.

[4] CIGRE TF-77, "VSC HVDC converters as virtual synchronous machine?," Sep. 2019. Accessed: Nov. 25, 2021. [Online]. Available: http://cigre.org/article/GB/news/the_latest_news/tf-77-vsc-hvdc-converters-as-virtual-synchronous-machine

[5] S. D'Arco, G. Guidi, and J. Suul, "Operation of a modular multilevel converter controlled as a virtual synchronous machine," in *Proc. IEEE Int. Power Electron. Conf.*, Niigata, Japan, 2018, pp. 782–789.

[6] Q.-C. Zhong and G. Weiss, "Synchronverters: Inverters that mimic synchronous generators," *IEEE Trans. Ind. Electron.*, vol. 58, no. 4, pp. 1259–1267, Apr. 2011.

[7] S. d'Arco, J. A. Suul, and O. B. Fosso, "Small-signal modelling and parametric sensitivity of a virtual synchronous machine," in *Proc. Power Syst. Comput. Conf.*, Wroclaw, Poland, 2014, pp. 1–9.

[8] E. Avdiaj, J. A. Suul, S. d'Arco, and L. Piegari, "A virtual synchronous machine-based control for eliminating DC-side power oscillations of three-phase VSCs under unbalanced grid voltages," in *Proc. IEEE 15th Int. Conf. Compat., Power Electron. Power Eng.*, Florence, Italy, 2021, pp. 1–6.

[9] S. d'Arco and J. A. Suul, "Improving the power reference tracking of virtual synchronous machines by feed-forward control," in *Proc. IEEE 19th Int. Power Electron. Motion Control Conf.*, Gliwice, Poland, 2021, pp. 102–107.

[10] O. Mo, S. d'Arco, and J. A. Suul, "Evaluation of virtual synchronous machines with dynamic or quasi-stationary machine models," *IEEE Trans. Power Electron.*, vol. 64, no. 7, pp. 5952–5962, Jul. 2017.

[11] *Technical Requirements for Grid Connection of High Voltage Direct Current Systems and Direct Current-Connected Power Park Modules*, VDE-AR-N 4131 Standard, Mar. 2019.

[12] J. Chen, F. Prystupczuk, and T. O'Donnell, "Use of voltage limits for current limitations in grid-forming converters," *CSEE J. Power Energy Syst.*, vol. 6, no. 2, pp. 259–269, Jun. 2020.

[13] H. H. Xin, L. B. Huang, L. Q. Zhang, Z. Wang, and J. B. Hu, "Synchronous instability mechanism of P-f-droop-controlled voltage source converter caused by current saturation," *IEEE Trans. Power Syst.*, vol. 31, no. 6, pp. 5206–5207, Nov. 2016.

[14] T. Qoria, F. Gruson, F. Colas, G. Denis, T. Prevost, and X. Guillaud, "Critical clearing time determination and enhancement of grid-forming converters embedding virtual impedance as current limitation algorithm," *IEEE Trans. Emerg. Sel. Top. Power Electron.*, vol. 8, no. 2, pp. 1050–1061, Jun. 2020.

[15] D. Pan, X. Wang, F. Liu, and R. Shi, "Transient stability of voltage-source converters with grid-forming control: A design-oriented study," *IEEE Trans. Emerg. Sel. Top. Power Electron.*, vol. 8, no. 2, pp. 1019–1033, Jun. 2020.

[16] VDE FNN, *Grid Forming Behavior of HVDC Systems and DC-Connected PPMs - Supplement to VDE-AR-N 4131 for Dynamic Frequency/Active Power Behavior and Dynamic Voltage Control Without Reactive Current Specification*, VDE FNN Guideline, Aug. 2020.

[17] *Wind Energy Generation Systems - Part 21-1: Measurement and Assessment of Electrical Characteristics - Wind Turbines*, IEC 61400-21-1:2019 Standard., May 2019.

[18] X. Xiong, C. Wu, B. Hu, D. Pan, and F. Blaabjerg, "Transient damping method for improving the synchronization stability of virtual synchronous generators," *IEEE Trans. Power Electron.*, vol. 36, no. 7, pp. 7820–7831, Jul. 2021.

[19] CIGRE WG B4.57, "Guide for the development of models for HVDC converters in a HVDC Grid," CIGRE, Paris, France, Tech. Rep. 604, 2014.

[20] *Int. Electrotechnical Commission (IEC), Insul. Co-Ordination–Part 4: Comput. Guide to Insul. Co-Ordination and Modelling of Elect. Psychon. Netw.*, 1st ed., IEC, Geneva, Switzerland, Tech. Rep. TR 60071-4, 2004.

[21] M. Goertz, S. Wenig, S. Beckler, C. Hirsching, M. Suriyah, and T. Leibfried, "Analysis of cable overvoltages in symmetrical monopolar and rigid bipolar HVDC configuration," *IEEE Trans. Power Del.*, vol. 35, no. 4, pp. 2097–2107, Aug. 2020.

[22] K. Sharifabadi, L. Harnefors, H.-P. Nee, S. Norrga, and R. Teodorescu, *Design, Control and Application of Modular Multilevel Converters for HVDC Transmission Systems*. Chichester, U.K.: Wiley, 2016.

[23] S. Wenig, M. Goertz, C. Hirsching, M. Suriyah, and T. Leibfried, "On full-bridge bipolar MMC-HVDC control and protection for transient fault and interaction studies," *IEEE Trans. Power Del.*, vol. 33, no. 6, pp. 2864–2873, Dec. 2018.

[24] J. Freytes, J. Li, G. de Preville, and M. Thouvenin, "Grid-forming control with current limitation for MMC under unbalanced fault ride-through," *IEEE Trans. Power Del.*, vol. 36, no. 3, pp. 1914–1916, Jun. 2021.
[25] A. Gonzalez-Cajigas, J. R. Perez, and E. Bueno, "Design and analysis of parallel-connected grid-forming virtual synchronous machines for island and grid-connected applications," *IEEE Trans. Power Electron*., vol. 37, no. 5, pp. 5107–5121, May 2022.
[26] X. Guo, W. Wu, and Z. Chen, "Multiple-complex coefficient-filter-based phase-locked loop and synchronization technique for three-phase grid-interfaced converters in distributed utility networks," *IEEE Trans. Ind. Electron.*, vol. 58, no. 4, pp. 1194–1204, Apr. 2011.
[27] S. Golestan, M. Monfared, and F. D. Freijedo, "Design-oriented study of advanced synchronous reference frame phase-locked loops," *IEEE Trans. Power Electron.*, vol. 28, no. 2, pp. 765–778, Feb. 2013.

Carolin Hirsching was born in Bietigheim-Bissingen, Germany, in 1993. She received the B.Sc. degree in electrical engineering in 2015 and the M.Sc. degree in electrical engineering in 2017 from the Karlsruhe Institute of Technology (KIT), Karlsruhe, Germany, where she is currently working toward the Ph.D. degree in electrical engineering. She is also a Research Associate with the Institute of Electric Energy Systems and High-Voltage Technology, KIT. Her research interests include MMC control strategies for embedded HVDC schemes, converter-driven stability, and AC/DC interactions. She is a Young Member of VDE and CIGRE.

Max Goertz was born in Ludwigshafen, Germany, in 1991. He received the M.Sc. and Dr.-Ing. degrees in electrical engineering from the Karlsruhe Institute of Technology, Karlsruhe, Germany, in 2015 and 2020, respectively. In the following, he was with the German TSO TransnetBW. He is currently a Co-founder and the Managing Director of Mosaic Grid Solutions GmbH, Karlsruhe, Germany, where he supports customers as a Senior Power System Consultant. His research interests include modeling of HVDC and FACTS systems for EMT-type studies, benchmark of grid-forming behavior, control and protection of power electronic assets, and insulation coordination of HVAC and HVDC equipment. He is a Member of VDE and CIGRE and participates in several CIGRE Expert Groups.

Simon Wenig (Member, IEEE) was born in Coburg, Germany, in 1985. He received the Dipl.-Ing. and Dr.-Ing. degrees in electrical engineering from the Karlsruhe Institute of Technology, Karlsruhe, Germany, in 2013 and 2019, respectively. From 2018 to 2022, he was with the German TSO TransnetBW. He is currently a Co-founder and Managing Director of Mosaic Grid Solutions GmbH, Karlsruhe, Germany, where he supports customers as a Senior Power System Consultant. His research interests include EMT-type grid integration studies and EMT tools, HVDC and FACTS controls and dynamic performance, and power-quality aspects of future grids. He is a Member of VDE and CIGRE and active in several international working Groups.

Alexander Bisseling was born in Baden-Baden, Germany, in 1994. He received the B.Sc. degree in electrical engineering in 2017 and the M.Sc. degree in electrical engineering in 2020 from the Karlsruhe Institute of Technology (KIT), Karlsruhe, Germany, where he is currently working toward the Ph.D. degree in electrical engineering. He is also a Research Associate with the Institute of Electric Energy Systems and High-Voltage Technology, KIT. His research interests include converter-driven stability, and AC/DC interactions and grid modelling.

Michael Suriyah (Member, IEEE) was born in Kuala Lumpur, Malaysia, in 1982. He received the Diploma and the M.Sc. degree in electrical engineering from the Karlsruhe University of Applied Sciences, Karlsruhe, Germany, in 2007 and 2008, respectively, and the Ph.D. degree in electrical engineering from the Karlsruhe Institute of Technology, Karlsruhe, Germany, in 2013. He is the Head of the Department for Power Networks with the Institute of Electric Energy Systems and High-Voltage Technology. His research interests include aging diagnostics and onsite testing of power transformers, high-voltage testing methods, analysis of electric power networks, and planning of future power systems. He is a Member of VDE.

Thomas Leibfried (Senior Member, IEEE) was born in Neckarsulm, Germany, in 1964. He received the Dipl.-Ing. and Dr.-Ing. degrees from the University of Stuttgart, Stuttgart, Germany, in 1990 and 1996, respectively. From 1996 to 2002, he was with the Siemens AG, Nuremberg, Germany, and currently with the power transformer business in various technical and management positions. In 2002, he joined the University of Karlsruhe (now KIT), Karlsruhe, Germany, as the Head of the Institute of Electric Energy Systems and High-Voltage Technology. He is a Member of VDE and CIGRE.